LA-UR-23-32495

Approved for public release; distribution is unlimited.

Title:	Detectors and diagnostics for multiprobe radiography using high-energy short-pulse lasers
Author(s):	Wang, Zhehui
Intended for:	Report Web
Issued:	2023-11-01

Detectors and diagnostics for multiprobe radiography using high-energy short-pulse lasers

Zhehui Wang, P-4, LANL; zwang@lanl.gov

(Updated: Oct. 10, 2023)

Multiprobe radiography requires the following diagnostic capabilities at minimum: radiographic source diagnostics, spectroscopy, imaging, and tomography diagnostics. Depending on the repetition rate of the radiation sources, the diagnostics may be a single-shot diagnostic, such as photographic (radiochromic and X-ray films for high energy photons) films, or a multiple-shot diagnostic for repetitive source operations, such as a high-speed framing camera. Due to the drastically different detector physics of electrons, photons at different energies (keV to 10s of MeV in the radiography context), heavy ions such as protons, alphas, and neutrons, see, for example, Ref. [1, 2] for an overview, different types or configurations of detectors and constructions may be required for multiprobe radiography applications. Some of the common detector metrics include, independent of the particle/photon species, sensitivities or efficiency, energy resolution, spatial or temporal resolutions and others. Some unique detection scenarios arise in a multiprobe radiography setting, for example, crosstalk mitigation and particle identification (ID) when X-ray and higher energy photons, relativistic electrons, neutrons, other hadrons, and heavy particles coexist at the detector location.

In terms of signal output, photographic films, CR-39 plastic, and image plates (IPs) can be characterized as non-electronic and passive types. These detectors, while older than electronic devices such as photo-diode arrays (PDAs), charge-coupled device (CCD) cameras, complementary metal-oxide semiconductor (CMOS) cameras, *etc*. are still used today due to, in part, their low cost, easy construction, design and configuration flexibility, large number of material choices, and/or relatively high immunity to electromagnetic pulses (EMP) and other laser-induced transients and background. For example, in comparison with a scintillator fiber detector with a CCD readout, IPs have several other advantages in a pulsed high-power laser environment [3]: the scanning size can be as small as 50 μm per pixel, which allows a much higher electron energy resolution than that of a scintillator array in a magnetic spectrometer, where each fiber is typically more than 500 μm in diameter. IPs are reusable and more cost effective. IPs do not require vacuum electrical feedthroughs or a cooling system, which is often used for a CCD to reduce the thermal noise at room temperature. Meanwhile, readout of photographic films, CR-39, and image plates requires additional steps such as chemical processing or a microscope or image plate scanner to convert the raw non-electronic signals into electronic formats, which are needed for computer processing of the data. These additional signal postprocessing steps may limit non-electronic detectors to single-shot experiments, with the exception when multiple pinholes or viewing angles are available, and time-gating of the signals is possible. As electronic devices such as CCD and CMOS cameras continue to improve in performance, including in spatial and temporal resolutions, sensitivity, and reduced noise [4], they are now gradually replacing the non-electronic detectors in the state-of-the-art ICF and HED experiments [5]. Bypassing the need for signal conversion in the electronic devices makes them particularly suitable for repetitive experiments with a short turn-around time, or for time-resolved multiprobe radiography. When scintillators are used for radiation detection, optical CCD and CMOS cameras are natural choices, serving both as the optical detectors and readout devices.

The radiographic source diagnostics share many common requirements and hardware with laser-driven ignition experiments such as NIF, OMEGA [6], and Z [5, 33], the three flagship HED facilities in the US, even though the optimization objectives may be slightly different. A recent collection of review articles on diagnostics for inertial confinement fusion [23] has rich information about ICF and HED diagnostics [24, 29, 34], analysis [32], imaging methods [28] and collaborations [5]. For multiprobe radiographic imaging applications, one optimization is towards better radiation sources including X-ray, electron, positron, proton or neutron yield at different energies, and directional emission towards the targets to be radiographed, while ignition experiments are tailored preferentially towards higher neutron yield, as a net result of nuclear fusion. The neutron, X-ray and γ-ray emissions are likely to be isotropic to the 0^{th} order in campaigns to optimize fusion yield.

Below we highlight various X-ray, neutron, electron, ion detectors that have proven use. Innovative combinations of these existing detectors, together with different radiation sources, may be the first steps in advancing multiprobe radiography and applications.

A bremsstrahlung X-ray spectrometer (BMXS) was developed, see Figure 1, to measure the hot electron energy distribution and to infer the hot electron temperature, which can be hundreds of keV in petawatt scale laser experiments. To measure the hot electron size, 2D images of Kα fluorescence from buried fluor layers were used to infer the hot electron source size at a given depth. Two techniques are currently used for 2D imaging: spherically bent Bragg crystals using a CCD or image plate detector and pinhole imaging using Ross pair [6b] filters using an image plate or gated scintillator detector.

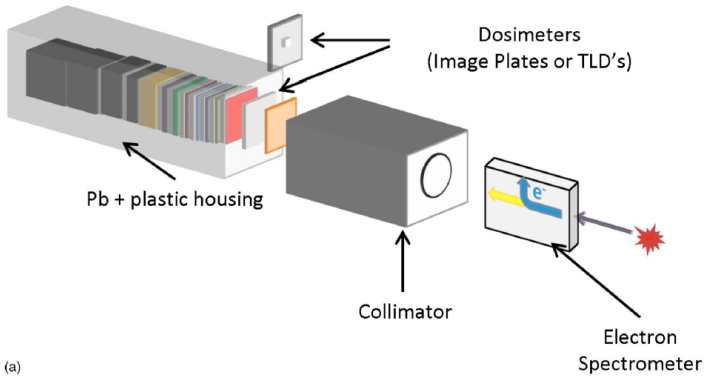

Figure 1. A bremsstrahlung spectrometer (BMXS) for hot electron energy distribution measurement. A differential Z filter stack within the Pb+plastic housing is designed to detect X-ray with hundreds of keV energy. The Monte Carlo code Integrated Tiger Series (ITS) was used to construct response matrices for both the target and the detector. Image adopted from Ref. [6].

For the symmetric implosion experiments in OMEGA using 60 beams, the temperature of the suprathermal electrons and the temporal dependence were measured with a time-resolved, four-channel hard X-ray detector (HXRD) [19] and two time-integrated imaging-plate diagnostics high-energy x-ray imager (HEXRI) [25] and BMXS [26]. Typical temperatures measured for the suprathermal electrons can be fit to single-temperature Maxwellian distributions with central temperatures in the range of 50 - 100 keV.

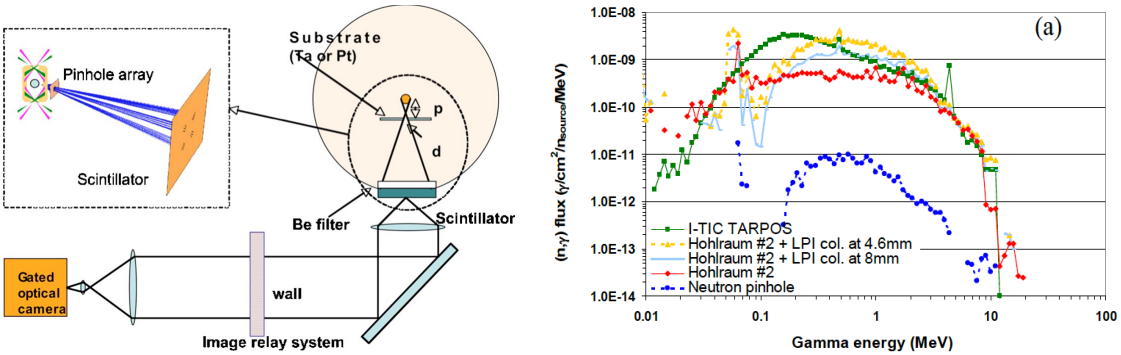

Figure 2. (Left) Simplified set up for the HEXRI [25]. (Right) (n,γ) flux in HEXRI detectors within a 50 ns window, per n source, per MeV, produced by the target positioner, hohlraum design #2, neutron pinhole, and hohlraum design #2 + LPI collimators [27].

Scintillators are used in gamma-ray and high-energy X-ray detectors [1, 48]. Effects of Cherenkov radiation is also explored for relativistic particles [20]. The High-Energy X-Ray Imager (HEXRI) system within the NIF facility is composed of two scintillators placed on the equatorial plane (θ=90º) at φ=89º and φ=348.7º, at 6 m from the target chamber center (outside the target chamber wall) [27]. A novel scintillator-based x-ray spectrometer for high-repetition-rate laser plasma interaction experiments were reported in [35].

Neutron action detectors are a class of passive detectors [1]. Many materials become radioactive (emitting alpha, beta or gamma-rays) or activated when exposed to neutrons [37]. Determination of neutron absorbed dose is made by measuring decay products of the activation foil (typically β- or γ-rays) using, for example, high-purity germanium detector. Neutron activation cross sections are material (isotope) and neutron energy sensitive. Many materials, such as H-1, Al-27, Fe-56, In-116m, Cu, V-52, Au-198, Sulfer-32, P-31, can be used as neutron activation detectors. In comparison with a camera which requires electricity to operate, a neutron activation detector is a simpler passive neutron-flux-integrating detector, and can be made very compact or large area (conform to the neutron flux). Meanwhile, the impurities of the activation materials can complicate the neutron-induced signal interpretation. In addition to neutron absorption cross section, selection of the neutron action materials also depends on the signal (β- or γ-rays) decay time. Neutron action detectors have limited use for time-resolved or high-repetition-rate measurements.

Neutron Imaging System (NIS) was designed for NIF led by LANL [38-40], and was based on the penumbral detection scheme [41]. NIS can detect both the primary 14 MeV neutrons and the lower-energy downscattered neutrons in the 6–13 MeV range. NIS, *Figure 4*, consists of an aperture array, alignment system, scintillator, data acquisition and analysis system, and the camera system. The camera system consists of the fiber optic and lens optical relays, the camera and the gated microchannel plate image intensifiers MCPII, and the charge coupled device (CCD). NIS uses a precisely aligned set of apertures near the target to form the neutron images on a segmented scintillator, 16 cm square BCF-99-55 scintillator that is 5 cm thick and composed of 250 μm diameter, 5 cm long round fibers. An earlier design used capillary array filled with a liquid scintillator [42], see Figure *3*.

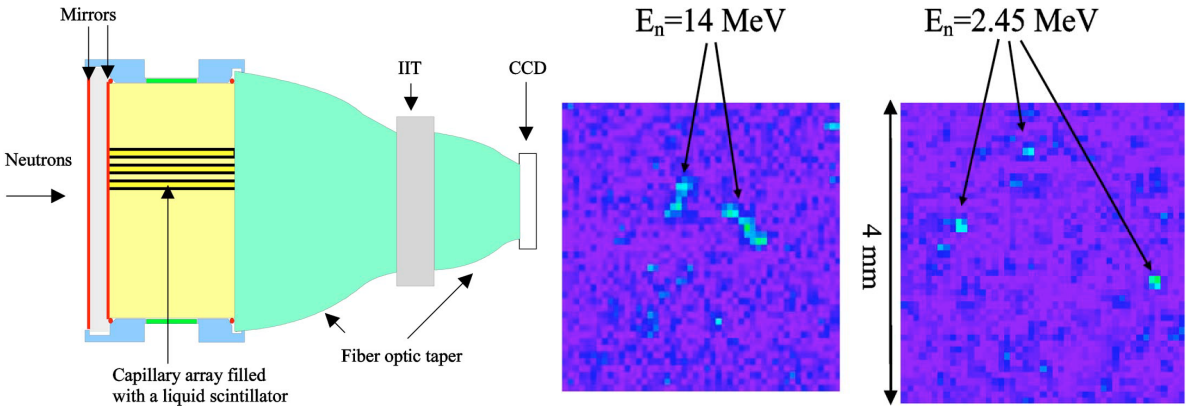

Figure 3. (Left) A neutron imaging device deployed in the OMEGA laser facility. (right) Recoil proton tracks produced when 14- and 2.45-MeV neutrons scatter hydrogen nuclei in the scintillator. Images adopted from [42].

The neutron point-spread function in NIS, calculated by using SCINFUL [31], can be fit by a double Gaussian with 0.021 and 0.284 mm sigma values. The images are recorded on a gated, intensified charge coupled device. Although the aperture set may be as close as 20 cm to the target, the imaging camera system will be located at a distance of 28 m from the target. At 28 m the camera system is outside the NIF building. Because of the distance and shielding, NIS is able to obtain images with little background noise. The imager is capable of imaging downscattered neutrons from failed capsules with yields greater than 10^{14} neutrons. The shielding also permits the NIS to function at neutron yields above 10^{18}, which is superior to most other diagnostics that may not work at high neutron yields, in particular when the NIF plasmas ignite.

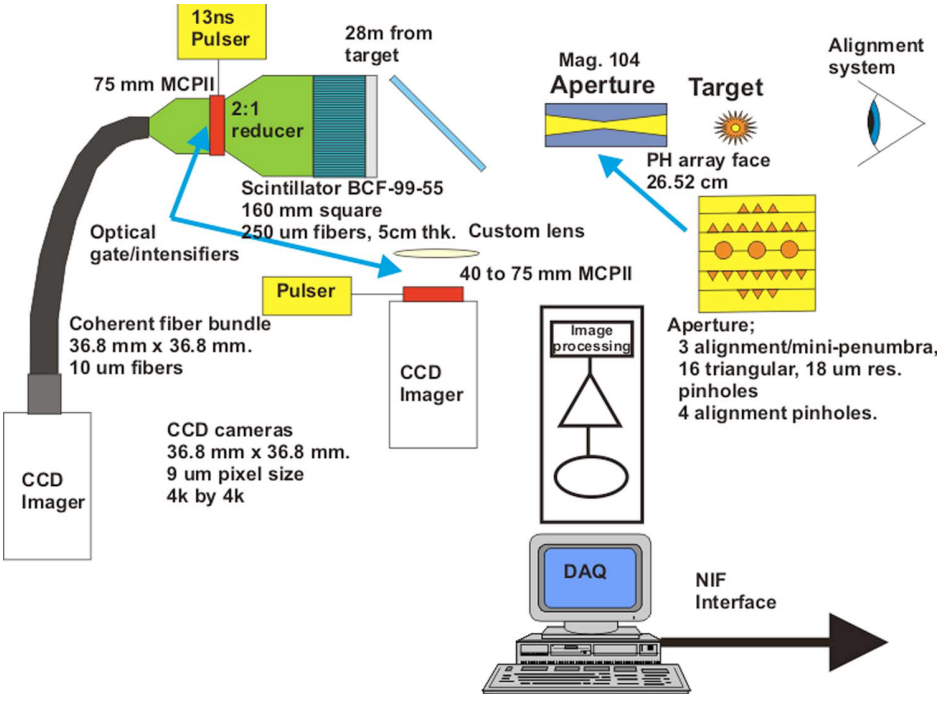

Figure 4. A schematic of the NIS system designed and built by LANL [40].

For a hit by a single 14 MeV neutron, about 180 photons leave the end of the 0.58 numerical aperture (NA) fiber in which the neutron interacted [40]. The reducer transmits a factor of 0.49 of the light to the MCPII because of the transmission loss and NA mismatch. The total number of photons per scintillator fiber reaching the MCPII is therefore 88, which results in roughly 8.8 photoelectrons per scintillator fiber per neutron. There are additional losses from coupling the MCPII phosphor to the CCD. However after the increase in the light per fiber from the MCPII, the further degradation of the DQE is minimal. The estimated DQE for detecting a single 14 MeV neutron at NIF is roughly 0.26. This number decreases for the lower energy neutrons that make up the downscattered image.

The fabrication and inspection of the NIS-3 neutron imaging aperture for the National Ignition Facility (NIF) prior to first use were completed in December 2018 [45]. The 16 layer aperture contains an array of 87 openings, manufactured by scribing 100 profiles along 20-cm lengths of thin gold foils. The openings consist of 15 penumbral and 72 triangular apertures. The 16 layers are then assembled into a single 15-mm x 16.6-mm x 200-mm component. Images produced from the array of apertures must be deconvolved in order to remove distortions caused by the extended length of the aperture. In order to deconvolve the image, the as-built aperture profile must first be characterized by measuring the scribed apertures at multiple places along their length.

Proton Beam Imaging Energy Spectrometer (PROBIES) is a simple repeating step-filtered structure for the detection of MeV-energy proton beams [46]. In contrast to CR-39 plastic detectors, which are passive MeV proton and heavy charged particle detectors and require chemical post-processing of signal and microscope readout, PROBIES can be fielded in with a scintillator and imaging setup to collect proton beam information in high-repetition rate experiments, Figure 5.

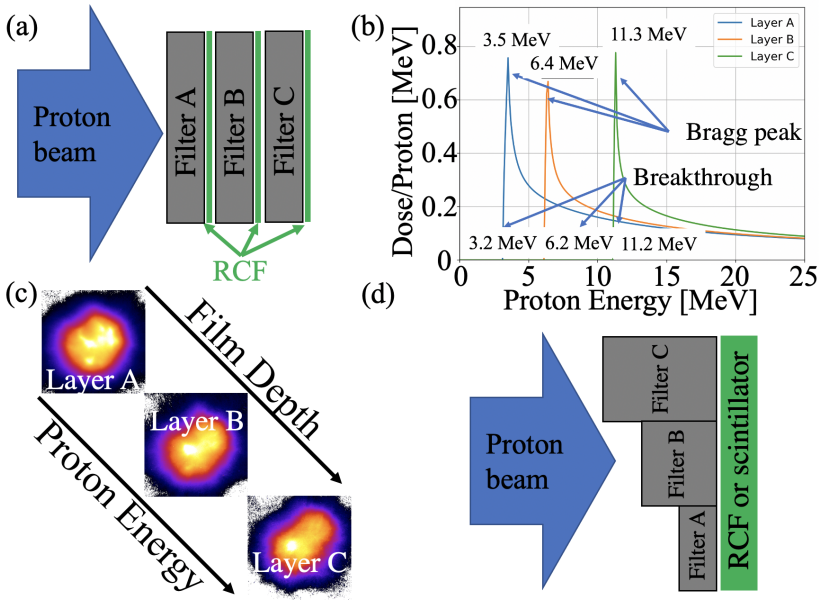

Figure 5. *Two PROBIES designs with a radiochromic film stack (RCF) and interleaving filters, (a); with scintillator or RCF on a single detector by spatially arranging filters of different thicknesses, (d); an example RCF stack response for a three film stack showing the minimum breakthrough energy and Bragg*

peak energies, (b); and Example of resulting proton beam data recorded on Radiochromic film (RCF) where films deeper in the stack record higher energy proton beam profiles, (c). Image adopted from [46].

Alternatively, inexpensive CMOS image sensor (CIS) detectors were demonstrated for real-time electron (beta-ray), heavy ions detection [47]. It was also shown that low-cost CIS are sensitive to MeV and higher energy protons and α-particles by using a ^{90}Sr β-source with its cover glass in place. Indirect, real-time, high-resolution detection is also feasible when combining CIS with a ZnS:Ag phosphor screen and optics. Noise reduction in CIS is nevertheless important for the indirect approach.

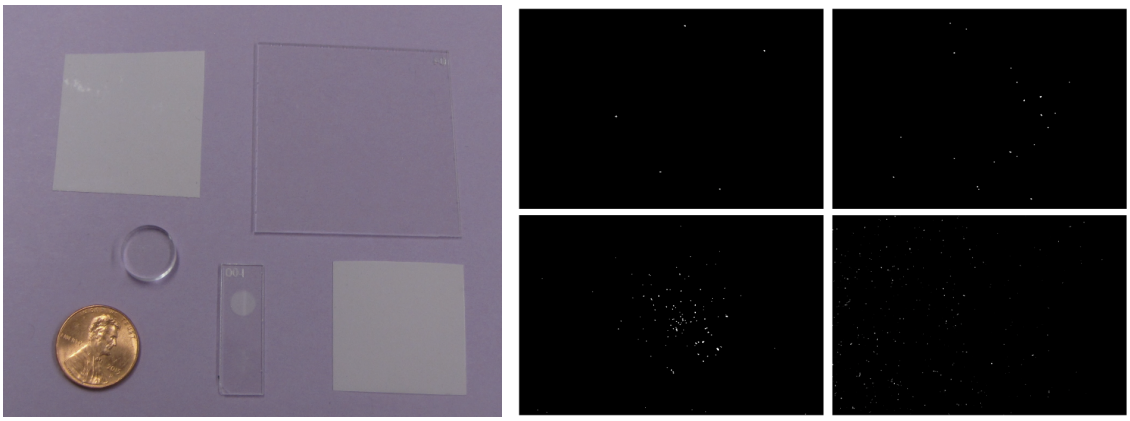

Figure 6. (Left) Selection of a thin ZnS:Ag phosphor screen (upper left corner) for the experiment. The objects shown from left to right, top to bottom, together with a US 1-cent coin are (a) a "half"-layer thick ZnS:Ag phosphor; (b) CR-39 not developed; (c) EJ-232Q-0.5%BZP plastic scintillator; (d) CR-39 developed after exposure to an 241Am for 10 s and 1 min (spot size = 6 mm); (e) a double-layer thick ZnS:Ag phosphor. (right) (a)-(c) Indirect detection of α's from an 241Am source using a Nikon D800 camera sensor at ISO of 640, 800, and 1000 for (a)-(c), respectively. (d) Direct detection of β's from a 90Sr source using a webcam CMOS sensor. Images adopted from [47].

Imaging plate detectors have been used for ion spectroscopy. A Thomson parabola ion spectrometer (TPIE) or Thomson spectrometer for ions has been designed and used to measure ions of different charge-to-mass ratios in multi-terawatt laser-driven experiments at the Laboratory for Laser Energetics (LLE) at the University of Rochester [7]. This device used parallel electric and magnetic fields to deflect particles of a given mass-to-charge ratio onto parabolic curves on the detector plane, see ***Figure 7*** for an illustration. Variations to this ion deflection design, such as wedge-shaped electrodes and overlapping electric and magnetic fields have since been introduced [8, 9].

The positions of the ions on the detector plane can be used to determine the ion energy. Fujifilm BAS-TR imaging plates was used as a detector in the Thomson parabola [7]. The imaging plate sensitivity was calibrated by using monoenergetic proton and alpha particle beams from the SUNY Geneseo 1.7 MV tandem Pelletron accelerator by National Electrostatics Corporation Model 5SDH [10], see ***Figure 8*** for an example. The monoenergetic particles range from 0.6 MeV to 3.4 MeV for protons and deuterons and from 0.9 MeV to 5.4 MeV for alpha particles.

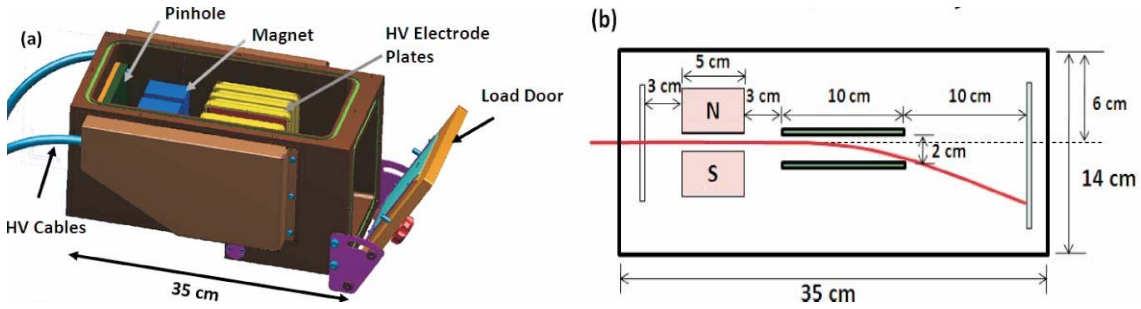

Figure 7. (a) Schematic of a Thomson Parabola ion spectrometer (TPIE) using parallel magnetic and electric fields to spatially disperse ions of different energies and charge-to-mass ratio. The load door is for inserting the ion detector, such as an imaging plate or a photographic (X-ray and others) film. (b) The key dimensions of the spectrometer and an example of an ion trajectory. *Figure adopted from [7].*

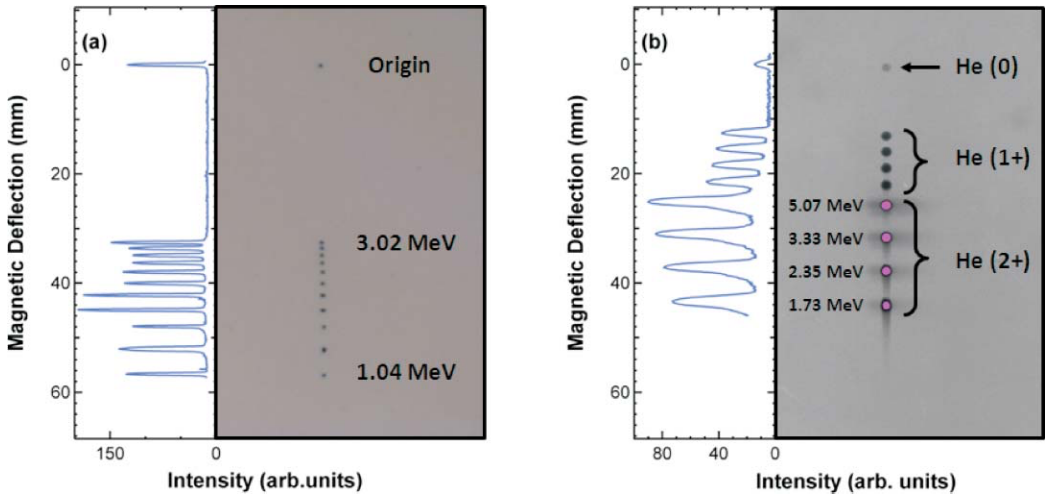

Figure 8. An example of Thomson parabola magnetic position calibration for different ions. (a) Proton data, in which radiochromic film was used on the detector plane. Figure (b) Alpha particle data, in which a Fujifilm imaging plate was used on the detector plane. Note that for a given exposure at a given energy, both the 1+ and 2+ charge states of helium-4 are clearly visible. *Figure adopted from [7].*

The response of imaging plates (IP) to protons of various energies reported in [7] was similar to the data reported previously by using ions produced by high-intensity lasers [11, 12]; however, the IP sensitivity reported here is 8%–37% lower than reported previously [11]. The principal difference was that the measurements in Ref. [7] were made using monoenergetic beams from an accelerator rather than ions produced in ultra-intense laser-matter interactions. Part of this discrepancy may be due to IP fading effect and/or differences in IP reader sensitivity. Ref. [7] also extended on the previous experiments by including IP sensitivity calibration for both deuterons and alpha particles.

MeV electrons, positrons, and protons can be produced when the laser intensity $I > 10^{19} / \lambda^2$ W cm^{-2} reaches a solid target. Here the laser wavelength λ is in μm. A series of low-cost compact electron and ion spectrometers were reported by using Fuji BAS SR2040 image plates as detectors [3, 13]. The spectrometers used permanent magnets, instead of electromagnets, to spatially

disperse electrons, positrons, and protons of different energies. Several versions have been developed by varying the magnetic field strength, ranging from hundreds of gausses to about 1 T. By changing the magnetic field strengths, the spectrometers can be tuned to measure electrons of 10's – 100's of keV, or at higher magnetic fields, measure MeV and higher energy electrons above 100 MeV. Examples of two versions of magnetic spectrometers using IPs, together with a scintillator and CCD based spectrometer are shown in *Figure 9*. Extensions of the work, modified electron-positron proton spectrometers (EPPS), have since been used in other facilities including OMEGA EP [14,15] and NIF, with applications to astrophysics [17].

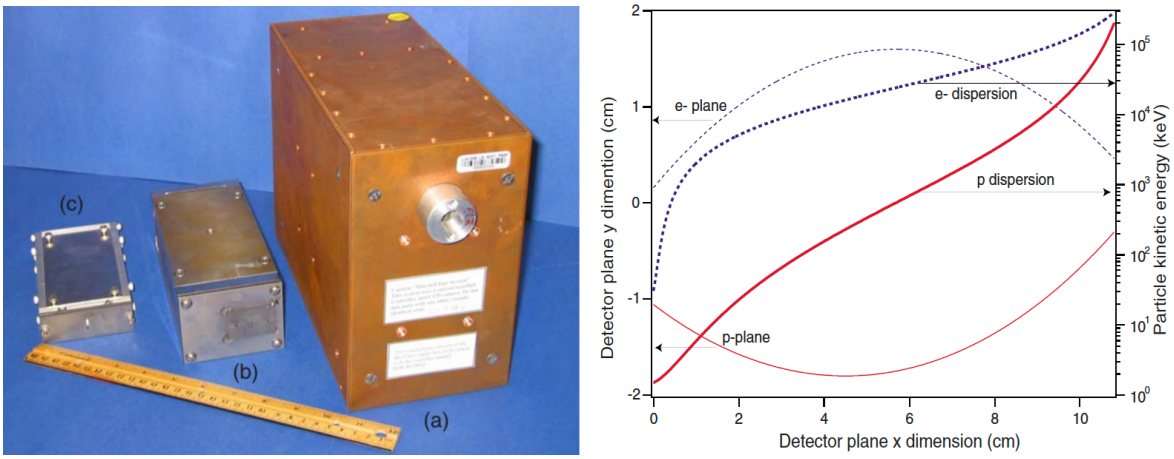

Figure 9. (Left) A comparison of three electron spectrometers developed at LLNL. (a) The scintillator-based spectrometer, which used a scintillating fiber array coupled to a fiber-front CCD camera. (b) The high-field that used image plate detector, and (c) A low-field magnetic spectrometers. (Right) A comparison of electron and proton dispersion in the spectrometer with a 0.8 T magnetic field. Images from Ref. [13].

A Dual-Channel Highly Ordered Pyrolytic Graphite (DC-HOPG) X-ray spectrometer was described for high energy short-pulse laser experiments [18]. The instrument used a pair of graphite crystals for two X-ray channels. A low energy "Cu channel" was optimized for self emission from low-Z materials, such as Cu Kα (8 keV), in first diffraction order and a high energy "Ag channel" was optimized for high-Z materials, such as Ag Kα (22 keV), in second diffraction order. The emissions from the target were detected using a pair of parallel imaging plates positioned in such a way, see *Figure 10*, that the noise from background is minimized and the mosaic focusing is achieved. BAS- MS 2040 imaging plates were used as detectors. After data acquisition, the imaging plates were scanned with Fuji FLA7000 scanner. The digitized images were then converted to Photo Stimulated Luminescence units (PSL) using the following formula given in the Fuji manuel.

Tests of the diagnostic on the Titan laser ($I \sim 10^{20}$ W/cm^2, $\tau = 0.7$ ps) showed excellent signal-to-noise ratio (SNR) > 1000 for the low energy channel and SNR > 400 for the high energy channel.

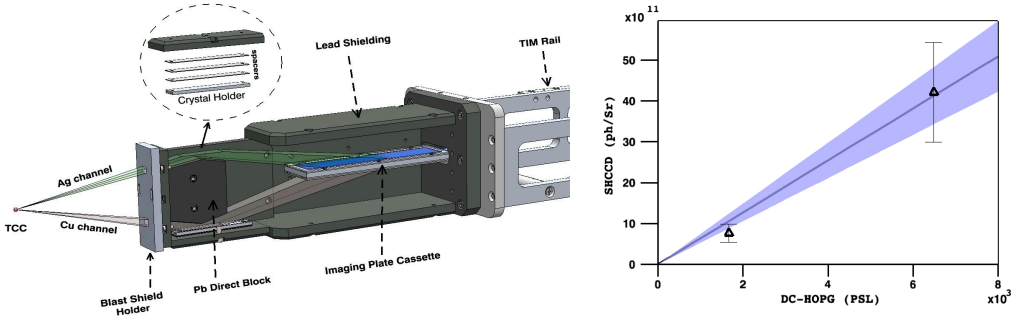

Figure 10. (Left) The layout of a Dual Channel Highly Ordered Pyrolytic Graphite (DC-HOPG) X-ray spectrometer. TIM stands for "Ten-inch manipulator". (Right) Calibration curve. DC-HOPG detector was calibrated against a single-hit CCD (SHCCD) detector. Image credit [18].

Gated microchannel plate (MCP) X-ray imaging has more than three decade of history and is now used at nearly every HED facility worldwide [5, 50]. Gating time as short as 30 ps was demonstrated in the 1990s. NIF currently has eight airbox gated MCP detectors operable in any DIM location [51]: four gated x-ray detectors (GXDs) with CCD readouts and four hardened GXDs (hGXDs) with film readout. OMEGA (LLE) now has eight gated x-ray framing cameras. Four are called X-ray framing camera (XRFC): two have 30 ps gating time and two have 100 ps gating time. Sydor Technologies, Inc offers XRFCs with fast or slow detection heads for frames ranging from 40 ps to 1000 ps in duration. OMEGA also has four single-frame cameras (SFCs) built by Sydor Technologies, Inc. The camera captures up to 16 sequential, temporally gated images, a short movie of nanosecond-scale phenomena. A streaked X-ray spectrometer was described in [30].

The X-ray emission from the center of the target can be measured temporally and spatially and spectrally resolved using an x-ray framing camera (XRFC) [21]. In an OMEGA-60 experiment [22], the XRFC spatially and temporally resolved the X-ray emission, using a 4 × 4 pinhole array to produce 16 enlarged images of the target on a microchannel-plate detector, which was covered with four strips of gold film. A 200-μm Be foil and a thin (12-μm) Ti foil placed in front of the detector, combined with the spectral response of the diagnostic, restricted the range of recorded X-rays to ~3 to 7 keV.

By using pulse-dilation technique, 5 ps gating resolution has been demonstrated [52]. DIlation X-ray Imager (DIXI) implemented pulse-dilation technique for high-speed X-ray framing camera at the National Ignition Facility (NIF). DIXI is sensitive to x-rays in the range of ~ 2 -17 keV [53]. The pulse-dilation technique allowed DIXI to achieve a temporal resolution of less than 10 ps, a ~ 10× improvement over conventional framing cameras that do not use electron pulse dilation technique on the NIF (≈100 ps resolution). Sub-ps temporal resolution was traditionally only attainable with 1D streaked imaging.

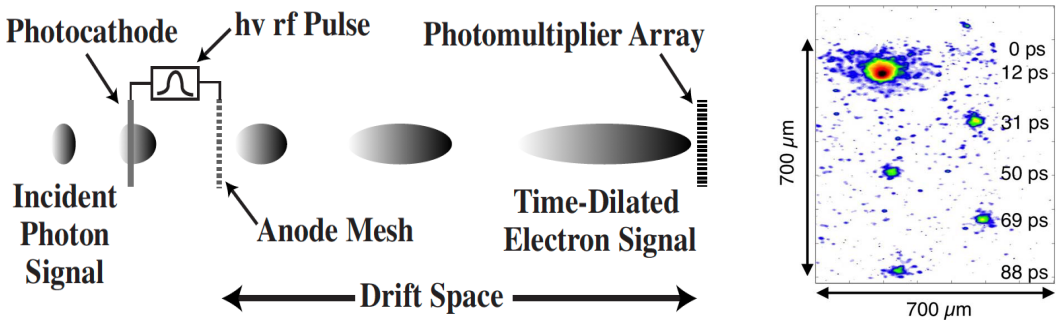

Figure 11. (Left) Pulse-dilation process starts with photoelectron generation from the photocathode when X-ray and other photons are intercepted. Photoelectrons are then accelerated with a time varying electric field (hv rf) and the resulting energy dispersion causes the signal to stretch axially as it traverses the drift region resulting in stretched electron pulsed before sampling by a gated microchannel plate or (PMT as indicated). Image from [52]. (right) Temporal evolution of the X-ray spot measured by DIXI from a titanium target by a TITAN laser, with 1 μm wavelength, 1 ps pulse duration, 100 J pulse energy and a focal spot of FWHM ≈15 μm. Image adopted From [53].

Some of the common issues or challenges with the multiprobe diagnostics including harsh radiation environment as the laser power and electric pulse power continue to increase. More X-rays, high-energy X-rays, neutrons, and energetic particles are generated experimentally, and most of them may not end up being detected. Furthermore, noise reduction, background subtraction, gain controls, higher detection sensitivity, particle identification, improvements in dynamic range, and improvements in resolution may be needed [1, 2].

There are ample opportunities for innovations as well, with detectors being an essential element. Multiprobe imaging and tomography can potentially obtain three-dimensional (3D) information with many different options in terms of multiple particle species, polychromatic or multi-energy particle spectra [2], which may be advantageous over single-probe mono-energetic sources. Polychromatic properties of the X-ray and high-energy X-ray sources alone offer attractive possibilities if the energy spectra of the sources can be controlled and measured with sufficient accuracy. For radiography of focused-scale experiments of ~1-10 g/cm^2 aerial densities using, for example, Colorado State's rep-rated laser, or Texas Petawatt, being able to deliver a known spectrum of MeV X-rays would be important [36]. In short, when detector innovations are coupled with source performance, data analysis, and different optimization schemes [54], *i.e.* by adopting the holistic approach [55], the *whole can exceed the sum of its parts* [5]. Additional factors, such as the cost and timeliness determined by project milestones and schedules, also need to be accounted for.

References:

[1] G. F. Knoll, Radiation Detection and Measurement, 4th ed., (Wiley, 2010).
[2] Zhehui Wang, Christophe Dujardin, Matthew S Freeman, Amanda E Gehring, James F Hunter, Paul Lecoq, Wei Liu, Charles L Melcher, CL Morris, Martin Nikl, Ghanshyam Pilania, Reeju Pokharel, Daniel G Robertson, Daniel J Rutstrom, Sky K Sjue, Anton S Tremsin, SA Watson, Brenden W Wiggins, Nicola M Winch, Mariya Zhuravleva, Needs,

trends, and advances in scintillators for radiographic imaging and tomography, IEEE Trans. Nucl. Sci. 70, 1244-1280 (2023). **DOI:** 10.1109/TNS.2023.3290826
[3] Hui Chen, Norman L. Back, Teresa Bartal, F. N. Beg, David C. Eder, Anthony J. Link, Andrew G. MacPhee, Yuan Ping, Peter M. Song , Alan Throop, and Linn Van Woerkom, Absolute calibration of image plates for electrons at energy between 100 keV and 4 MeV, Review of Scientific Instruments 79(4), 033301 (2008). DOI: 10.1063/1.2885045.
[4] Zhehui Wang, Kaitlin Anagnost, Cris W Barnes, Dana Mcgraw Dattelbaum, Eric R Fossum, Eldred Lee, Jifeng Liu, JJ Ma, William Zachary Meijer, Wanyi Nie, Christine Marie Sweeney, Audrey C Therrien, Hsinhan Tsai, Xin Yue, Billion-pixel x-ray camera (BiPC-X), Review of Scientific Instruments 92(4), 043708 (2021). DOI: 10.1063/5.0043013.
[5] J. D. Kilkenny, W. W. Hsing, S. H. Batha, G. A. Rochau, T. C. Sangster, P. M. Bell, D. K. Bradley, H. Chen, J. A. Frenje, M. Gatu-Johnson, V. Yu. Glebov, R. J. Leeper, A. J. Mackinnon, S. P. Regan, J. S. Ross, and J. l. Weaver, National Diagnostic Working Group (NDWG) for inertial confinement fusion (ICF)/high-energy density (HED) science: The whole exceeds the sum of its parts, Rev. Sci. Instrum. 94, 081101 (2023). DOI: 10.1063/5.0128650.
[6] A. G. MacPhee, K. U. Akli, F. N. Beg, C. D. Chen, H. Chen, R. Clarke, D. S. Hey, R. R. Freeman, A. J. Kemp, M. H. Key, J. A. King, S. Le Pape, A. Link, T. Y. Ma, H. Nakamura, D. T. Offermann, V. M. Ovchinnikov, P. K. Patel, T. W. Phillips, R. B. Stephens, R. Town, Y. Y. Tsui, M. S. Wei, L. D. Van Woerkom, and A. J. Mackinnon, *Review of Scientific Instruments* 79, 10F302 (2008).
[6b] P. A. Ross, Phys. Rev. 28, 425 (1926).
[7] C. Freeman, G. Fiksel, C. Stoeckl, N. Sinenian, M. Canfield, G. Graeper, A. Lombardo, C. Stillman, S. Padalino, C. Mileham, T. Sangster, and J. Frenje, "Calibration of a Thomson parabola ion spectrometer and fujifilm imaging plate detectors for protons, deuterons, and alpha particles," *Review of Scientific Instruments* 82 (7), *073301 (2011)*. DOI: 10.1063/1.3606446.
[8] S. Bandyopadhyay, D. Neely, G. Gregori, D. Carroll, P. McKenna, M. Borghesi, F. Lindau, O. Lundh, C. Wahlström, and A. Higginbotham, "Analysis on a wedge-shaped Thomson spectrometer for ion studies," tech. rep., Technical Report 1, Central Laser Facility, CCLRC Rutherford Appleton Lab, 2005.
[9] J. Cobble, K. Flippo, D. Offermann, F. Lopez, J. Oertel, D. Mastrosimone, S. Letzring, and N. Sinenian, "High-resolution thomson parabola for ion analysis," Review of Scientific Instruments, 82 (11), 113504, 2011.
[10] SUNY Geneseo facility, https://www.geneseo.edu/physics/nuclear.
[11] A. Mancic, J. Fuchs, P. Antici, S. A. Gaillard, and P. Audebert, Rev. Sci. Instrum. 79, 073301 (2008).
[12] S. Taniguchi, A. Yamadera, T. Nakamura, and A. Fukumura, Nucl. Instrum. Methods Phys. Res. A 413, 119 (1998).
[13] H. Chen, A. J. Link, R. van Maren, P. K. Patel, R. Shepherd, S. C. Wilks, and P. Beiersdorfer, "High performance compact magnetic spectrometers for energetic ion and electron measurement in ultraintense short pulse laser solid interactions," Review of Scientific Instruments 79 (10), 10E533 (2008).
[14] J. L. Shaw, M. A. Romo-Gonzalez, N. Lemos, P. M. King, G. Bruhaug, K. G. Miller,C. Dorrer, B. Kruschwitz, L. Waxer, G. J. Williams, M. V. Ambat, M. M. McKie, M. D. Sinclair,

W. B. Mori, C. Joshi, Hui Chen, J. P. Palastro, F. Albert & D. H. Froula, Scientific Reports | (2021) 11:7498. https://doi.org/10.1038/s41598-021-86523-5
[15] G. Bruhaug, M. S. Freeman, H. G. Rinderknecht, L. P. Neukirch, C. H. Wilde, F. E. Merrill, J. R. Rygg, M. S. Wie, G. W. Collins & J. L. Shaw, Single-shot electron radiography using a laser-plasma accelerator, Scientific Reports | (2023) 13:2227.
[17] H. Chen and F. Fiuza, Perspectives on relativistic electron–positron pair plasma experiments of astrophysical relevance using high-power lasers, Phys. Plasmas 30, 020601 (2023). doi: 10.1063/5.0134819
[18] K. U. Akli, P. K. Patel, R. Van Maren, R. B. Stephens, M. H. Key, D. P. Higginson, B. Westover, C. D. Chen, A. J. Mackinnon, T. Bartal, F. N. Beg, S. Chawla, R. Fedosejevs, R. R. Freeman, D. S. Hey, G. E. Kemp, S. LePape, A. Link, T. Ma, A. G. MacPhee, H. S. McLean, Y. Ping, Y. Y. Tsui, L. D. Van Woerkom, M. S. Wei, T. Yabuuchi, and S. Yuspeh, "A dual channel x-ray spectrometer for fast ignition research," Journal of Instrumentation 5 (07), P07008 (2010).
[19] C. Stoeckl, V. Y. Glebov, D. D. Meyerhofer, W. Seka, B. Yaakobi, R. P. J. Town, and J. D. Zuegel, Rev. Sci. Instrum. 72, 1197 (2001).
[20] Y. Kim; H. W. Herrmann, Gamma-ray measurements for inertial confinement fusion applications, Rev. Sci. Instrum. 94, 041101 (2023)
[21] D. K. Bradley, P. M. Bell, J. D. Kilkenny, R. Hanks, O. Landen, P. A. Jaanimagi, P. W. McKenty, and C. P. Verdon, Rev. Sci. Instrum. 63, 4813 (1992).
[22] R. Nora, W. Theobald, R. Betti, F. J. Marshall, D. T. Michel, W. Seka, B. Yaakobi, M. Lafon, C. Stoeckl, J. Delettrez, A. A. Solodov, A. Casner, C. Reverdin, X. Ribeyre, A. Vallet, J. Peebles, F. N. Beg, and M. S. Wei, Gigabar Spherical Shock Generation on the OMEGA Laser, Phys. Rev. Lett. 114, 045001 (2015).
[23] S. Batha (Guest Editor), Diagnostics for inertial confinement fusion, https://pubs.aip.org/rsi/collection/1610/Diagnostics-for-inertial-confinement-fusion
[24] A. S. Moore; D. J. Schlossberg; B. D. Appelbe; G. A. Chandler; A. J. Crilly; M. J. Eckart; C. J. Forrest; V. Y. Glebov; G. P. Grim; E. P. Hartouni; R. Hatarik; S. M. Kerr; J. Kilkenny; J. P. Knauer, Neutron time of flight (nToF) detectors for inertial fusion experiments, Rev. Sci. Instrum. 94, 061102 (2023).
[25] R. Tommasini, J. A. Koch, B. Young, E. Ng, T. Phillips, and L. Dauffy, Rev. Sci. Instrum. 77, 10E301 (2006).
[26] C. D. Chen, J. A. King, M. H. Key, K. U. Akli, F. N. Beg, H. Chen, R. R. Freeman, A. Link, A. J. Mackinnon, A. G. MacPhee et al., Rev. Sci. Instrum. 79, 10E305 (2008).
[27] L Dauffy, R Tommasini, N Izumi, S Hatchett, P Song, Nino Landen, 2008 J. Phys.: Conf. Ser. 112 032085.
[28] David S. Montgomery, Invited article: X-ray phase contrast imaging in inertial confinement fusion and high energy density research, Rev. Sci. Instrum. 94, 021103 (2023).
[29] J. L. Porter, Q. Looker, L. Claus, Hybrid CMOS detectors for high-speed X-ray imaging, Rev. Sci. Instrum. 94, 061101 (2023)
[30] M. Millecchia, S. P. Regan, R. E. Bahr, M. Romanofsky, and C. Sorce, Rev. Sci. Instrum. 83, 10E107 (2012).
[31] J. K. Dickens, Oak Ridge National Laboratory, Report No. ORNL-6462, March 1988.
[32] P. F. Knapp; W. E. Lewis, Advanced data analysis in inertial confinement fusion and high energy density physics, 10.1063/5.0128661.

[33] T. J. Webb, D. E. Bliss, G. A. Chandler, D. H. Dolan, G. Dunham, A. Edens, E. Harding, M. D. Johnston, M. C. Jones, S. Langendorf, M. Mangan, A. J. Maurer, C. A. McCoy, N. W. Moore, R. Presura, A. M. Steiner, M. Wu, D. A. Yager-Elorriaga, and K. C. Yates, Radiation, optical, power flow, and electrical diagnostics at the Z facility: Layout and techniques utilized to operate in the harsh environment, Rev. Sci. Instrum. 94, 031102 (2023).
[34] A. S. Moore; D. J. Schlossberg; B. D. Appelbe; G. A. Chandler; A. J. Crilly; M. J. Eckart; C. J. Forrest; V. Y. Glebov; G. P. Grim; E. P. Hartouni; R. Hatarik; S. M. Kerr; J. Kilkenny; J. P. Knauer, Neutron time of flight (nToF) detectors for inertial fusion experiments, Rev. Sci. Instrum. 94, 061102 (2023).
[35] D. R. Rusby; C. D. Armstrong; C. M. Brenner; R. J. Clarke; P. McKenna; D. Neely, Novel scintillator-based x-ray spectrometer for use on high repetition laser plasma interaction experiments, Rev. Sci. Instrum. 89, 073502 (2018).
[36] J. Strehlow, private conversation.
[37] K. Hossny, Ahmad Hany Hossny, S. Magdi, Abdelfattah Y. Soliman & Mohammed Hossny, Detecting shielded explosives by coupling prompt gamma neutron activation analysis and deep neural networks, Sci. Rep. (2020) 10:13467.
[38] C. R. Christensen, Cris W. Barnes, G. L. Morgan, M. Wilke, and D. C. Wilson, First results of pinhole neutron imaging for inertial confinement fusion, Rev. Sci. Instrum. 74, 2690 (2003)
[39] F. E. Merrill; D. Bower; R. Buckles; D. D. Clark; C. R. Danly; O. B. Drury; J. M. Dzenitis; V. E. Fatherley; D. N. Fittinghoff; R. Gallegos; G. P. Grim; N. Guler; E. N. Loomis; S. Lutz; R. M. Malone; D. D. Martinson; D. Mares; D. J. Morley; G. L. Morgan; J. A. Oertel; I. L. Tregillis; P. L. Volegov; P. B. Weiss; C. H. Wilde; D. C. Wilson, The neutron imaging diagnostic at NIF (invited), Rev. Sci. Instrum. 83, 10D317 (2012).
[40] Mark D. Wilke; Steven H. Batha; Paul A. Bradley; Robert D. Day; David D. Clark; Valerie E. Fatherley; Joshua P. Finch; Robert A. Gallegos; Felix P. Garcia; Gary P. Grim; Steven A. Jaramillo; Andrew J. Montoya; Michael J. Moran; George L. Morgan; John A. Oertel; Thomas A. Ortiz; Jeremy R. Payton; Peter Pazuchanics; Derek W. Schmidt; Adelaida C. Valdez; Carl H. Wilde; Doug C. Wilson, The National Ignition Facility Neutron Imaging System, *Rev. Sci. Instrum*. **79**, 10E529 (2008).
[41] D. Ress, R. A. Lerche, R. J. Ellis, S. M. Lane, and K. A. Nugent, Science 241, 956–958 (1988).
[42] L. Disdier, L. Disdier, A. Rouyer, I. Lantuéjoul, O. Landoas, J. L. Bourgade, T. C. Sangster, V. Yu. Glebov, R. A. Lerche, Inertial confinement fusion neutron images, Phys. Plasmas 13, 056317 (2006).
[45] V.E. Fatherley, L.A. Goodwin, D.W. Schmidt, S.H. Batha, N. L. Cordes, V. Geppert-Kleinrath, H.J. Jorgenson, J.I. Martinez, T. J. Murphy, J.A. Oertel, M.P. Springstead, C.A. Wilde, P.L. Volegov, *Three-dimensional characterization of the third line-of-site neutron imaging pinhole at NIF,* Proc. SPIE 11114, Hard X-Ray, Gamma-Ray, and Neutron Detector Physics XXI, 1111412 (9 September 2019); doi: 10.1117/12.2529516.
[46] D. A. Marisca, B. Z. Djordjev´ıc, E. S. Grace, R. Hollinger, T. Ma, G. G. Scott, H. Song, R. A. Simpson, J. J. Rocca, and S. Wang, Design of Flexible Proton Beam Imaging Energy Spectrometers (PROBIES), *Plasma Physics and Controlled Fusion* 63 114003 (2021).
[47] Kenie Omar Plaud-Ramos, Matthew Stouten Freeman, Wanchun Wei, Elena Guardincerri, Jeffrey Darnell Bacon, J Cowan, J Matthew Durham, Di Huang, Jun Gao, Mark Arles Hoffbauer, Deborah Jean Morley, Christopher L Morris, Daniel Cris Poulson, Zhehui Wang,

A study of CR-39 plastic charged-particle detector replacement by consumer imaging sensors, Rev. Sci. Instrum. 87, 11E706 (2016).
[48] E. Liang; K. Q. Zheng; K. Yao; W. Lo; H. Hasson; A. Zhang; M. Burns; W. H. Wong; Y. Zhang; A. Dashko; H. Quevedo; T. Ditmire; G. Dyer, A scintillator attenuation spectrometer for intense gamma-rays, Rev. Sci. Instrum. 93, 063103 (2022).
[50] M. Koga, T. Fujiwara, T. Sakaiya, M. Lee, K. Shigemori, H. Shiraga, and H. Azechi, Rev. Sci. Instrum. 79, 10E909 (2008).
[51] J. A. Oertel, R. Aragonez, T. Archuleta, C. Barnes, L. Casper, V. Fatherley, T. Heinrichs, R. King, D. Landers, F. Lopez, P. Sanchez, G. Sandoval, L. Schrank, P. Walsh, P. Bell, M. Brown, R. Costa, J. Holder, S. Montelongo, and N. Pederson, Rev. Sci. Instrum. 77, 10E308 (2006).
[52] T. J. Hilsabeck, J. D. Hares, J. D. Kilkenny, P. M. Bell, A. K. L. Dymoke-Bradshaw, J. A. Koch, P. M. Celliers, D. K. Bradley, T. McCarville, M. Pivovaroff, R. Soufli, and R. Bionta, Pulse-dilation enhanced gated optical imager with 5 ps resolution (invited), REVIEW OF SCIENTIFIC INSTRUMENTS 81, 10E317 (2010).
[53] S. R. Nagel, T. J. Hilsabeck, P. M. Bell, D. K. Bradley, M. J. Ayers, K. Piston, B. Felker, J. D. Kilkenny, T. Chung, B. Sammuli, J. D. Hares, and A. K. L. Dymoke-Bradshaw, Investigating high speed phenomena in laser plasma interactions using dilation x-ray imager (invited), *Rev. Sci. Instrum.* 85, 11E504 (2014).
[54] Z. Wang, Radiographic imaging and tomography, Applied Optics 61 (6), RDS1-RDS4 4 (2022).
[55] Zhehui Wang, Andrew FT Leong, Angelo Dragone, Arianna E Gleason, Rafael Ballabriga, Christopher Campbell, Michael Campbell, Samuel J Clark, Cinzia Da Và, Dana M Dattelbaum, Marcel Demarteau, Lorenzo Fabris, Kamel Fezzaa, Eric R Fossum, Sol M Gruner, Todd Hufnagel, Xiaolu Ju, Ke Li, Xavier Llopart, Bratislav Lukić, Alexander Rack, Joseph Strehlow, Audrey C Therrien, Julia Thom-Levy, Feixiang Wang, Tiqiao Xiao, Mingwei Xu, Xin Yue, Nuclear Instruments and Methods in Physics Research Section A: Accelerators, Spectrometers, Detectors and Associated Equipment 1057, 168690 (2023).